

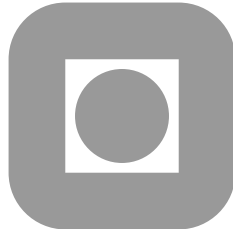
NORGES TEKNISK-NATURVITENSKAPELIGE
UNIVERSITET

**On pattern selection in three-dimensional
Bénard-Marangoni flows**

by

Arne Morten Kvarving, Tormod Bjøntegaard, Einar M. Rønquist

PREPRINT
NUMERICS NO. 4/2010



NORWEGIAN UNIVERSITY OF
SCIENCE AND TECHNOLOGY
TRONDHEIM, NORWAY

This report has URL

<http://www.math.ntnu.no/preprint/numerics/2010/N4-2010.pdf>

Address: Department of Mathematical Sciences, Norwegian University of Science and
Technology, N-7491 Trondheim, Norway.

On pattern selection in three-dimensional Bénard-Marangoni flows

Arne Morten Kvarving, Tormod Bjøntegaard, Einar M. Rønquist

October 7, 2010

In this paper we study Bénard-Marangoni convection in confined containers where a thin fluid layer is heated from below. We consider containers with circular, square and hexagonal cross-sections. For Marangoni numbers close to the critical Marangoni number, the flow patterns are dominated by the appearance of the well-known hexagonal convection cells. The main purpose of this computational study is to demonstrate the importance of the initial conditions on the pattern selection. In a series of numerical experiments, the coupled fluid-thermal system is started with a zero initial condition for the velocity and a random initial condition for the temperature. We demonstrate that the system can end up in more than one state. For example, the final state of the system may be dominated by a steady convection pattern with a fixed number of cells, however, the same system may occasionally end up in a steady pattern involving a slightly different number of cells, or it may end up in a state where most of the cells are stationary, while one or more cells end up in an oscillatory state. For larger aspect ratio containers, we are also able to reproduce dislocations in the convection pattern, which have also been observed experimentally. It has been conjectured that such imperfections (e.g., a localized star-like pattern) are due to small irregularities in the experimental setup (e.g., the geometry of the container). However, we show, through controlled numerical experiments, that such phenomena may appear under otherwise ideal conditions. By repeating the numerical experiments for the same non-dimensional numbers, using a different random initial condition for the temperature in each case, we are able to get an indication of how rare such events are. Next, we study the effect of symmetrizing the initial conditions. Finally, we study the effect of selected geometry deformations on the resulting convection patterns.

Keywords: Bénard-Marangoni, spectral elements, pattern formation

1 Introduction

We consider Bénard-Marangoni convection in confined containers where a thin fluid layer is heated from below. This problem has previously been studied extensively, both experimentally as well as computationally. An intriguing feature of this problem is the formation of hexagonal convection cells from random initial conditions; see [2, 22, 17]. It has been found that this formation can originate from two different effects; it can be caused by buoyancy effects due to the fact that the density is a function of the temperature, or it can be due

to variations in the surface tension, i.e., thermocapillary forces. Both effects can also be present at the same time. In fact, the concurrent presence of the two effects was a source of confusion for years. Bénard himself had an incorrect interpretation of which effect was the dominant one in his original experiments [2], which lead to Rayleigh’s subsequent stability analysis also being done under the assumption of buoyancy-driven convection [34]. It took several decades before this misunderstanding was cleared up; see [7, 32, 39].

The benchmark experiments in later years have been those of Koschmieder and Prahl [24]. In his monograph [22], Koschmieder gives a comprehensive overview of the problem, both from a theoretical and experimental point of view.

Ramon et al [33] investigated the pattern formation predicted for small aspect ratio containers. They obtained results that confirmed the predictions made by Rosenblat et al [35] based on linear stability theory.

Yu et al [43] studied the pattern formation computationally using a least-squares finite-element-based method. Their focus was on reproducing the experimental results due to Koschmieder [22]. They obtained results which were in good agreement, both at the qualitative level, reproducing the patterns from the experiments, as well as predicting the critical Marangoni numbers. Their simulations were started with an initial condition consisting of a superposition of all Fourier modes that were resolved on their grids.

Dauby et al [13] used a spectral Tau method to determine the critical Marangoni number, as well as the convective pattern at the threshold. The simulations were performed for rectangular containers with rigid walls, with the aspect ratio as the main parameter. The influence of a non-vanishing gravity and a non-zero Biot number at the free surface was examined. The authors showed that the convective pattern above the threshold may differ substantially from the pattern predicted from linear stability theory due to the presence of the rigid walls. In a follow-up study [14] the linear instability in circular containers were investigated. The authors numerically confirmed the principle of “exchange of stabilities” [15].

In a more recent study [30], Medale and Cerisier investigated numerically the convection patterns in containers of various shapes and sizes using a finite volume method. They also found results which were in very good agreement with the experimental results from [24].

Bjøntegaard and Rønquist [6] studied numerically the effects of a deformable free surface using a high order spectral element method. The deformations were found to be small with an amplitude varying linearly with the capillary number. This is in good agreement with the analysis done in [37]. The flow pattern was found to be mostly unaffected by the deformation, which means that the errors incurred by modelling the free surface as flat can be ignored for applications considering pattern formations. This confirms the theoretical results from several analyses, such as those found in [16, 25, 38].

As previously mentioned, the flow tends to organize in hexagonal cells for Marangoni numbers close to the critical number. Since a linear analysis cannot predict the shape of the cells, Cloot and Lebon performed a nonlinear analysis in an attempt to explain why the hexagonal shape seems to be preferred [12]. They investigated how different cell structures (triangular, square, pentagonal, hexagonal) behave with respect to perturbations. They found that indeed only a hexagonal flow pattern is stable with respect to perturbations of other shapes. If the triangular, square or pentagonal cells were perturbed with a hexagonal pattern, the original pattern eventually broke down and the system evolved into a new configuration which was dominated by hexagonal cells. This seems to confirm that in the supercritical regime, where instabilities have been triggered, we would expect a flow dominated by hexagonal cells, possibly with a few exceptions near the boundaries where wall effects play a significant role, and this is exactly what is observed in most experiments

and computations. It turns out that this is only part of the overall picture. Nitschke and Thess showed experimentally [31] the existence of a secondary instability for large temperature differences. This instability seems to break the stability of the hexagonal cells and instead drives the flow towards a pattern dominated by square cells. Their findings were numerically confirmed in a DNS performed by Bestehorn [3]. He was able to show that this instability is only present for a finite Prandtl number, and that the strength of the secondary instability increases for decreasing Prandtl numbers.

Other deviations from a hexagonal pattern are dislocations observed experimentally even in the weakly supercritical regime; in this case cells which are pentagonal, square or even triangular in shape appear; see Figure 1. Koschmieder et al briefly comment on this in [23] where they speculate that the defects are caused by impurities in the experimental setup, although they were never able to locate any impurities. Cerisier et al attempted to get some quantitative data on this through statistical analysis of experimental data in [9] and from a topological analysis in [10]. They found that the pattern defects follow many well established topological laws from other physical systems. However, they could not find any statistically significant influence of the initial conditions on the pattern dynamics when the initial conditions were seeded with either triangular patterns, square patterns or pentagonal patterns, reassuring the predictions from [12].

A lot of data about the defects and their formation is available. However, we have not been able to find a satisfactory explanation in the literature concerning the appearance of such defects well below the threshold of the secondary instability. We intend to see if it is possible to reproduce such defects in our computations. In particular, we investigate the effect of using different initial conditions on the pattern formation. We also examine the effect of imposing selected geometry deformations. An obvious advantage numerical tests have over experiments is the fact that we do not have to worry about the influence of measurement errors or imperfect geometries.

The governing equations for this problem are the incompressible Navier-Stokes equations coupled with a convection-diffusion equation for the temperature. The solution to this problem (velocity, temperature and pressure) is expected to be of high regularity and thus high order spatial discretizations [28] should be very attractive to use for this class of application. Combined with the solution algorithms recently developed for “extruded” three-dimensional domains [4], our computational approach help us to more easily consider larger systems and make it more feasible to perform repeated computations with different initial conditions.

The outline of the paper is as follows. In Section 2, we present the governing equations in strong form for the coupled fluid-thermal problem; the corresponding weak form is given in Section 3. The discretization is briefly outlined in Section 4. In Section 5, we present numerical results verifying the correctness of the fully discrete model by considering a number of complimentary test problems. In Section 6, we study the pattern formation resulting from random initial conditions. Several statistical series of tests are performed in order to demonstrate the possible states the system may end up in, and also to reproduce dislocations in the patterns which are also observed experimentally. In Section 7, we consider the effect of using slightly deformed containers. Finally, in Section 8, we summarize our findings and present our conclusions.

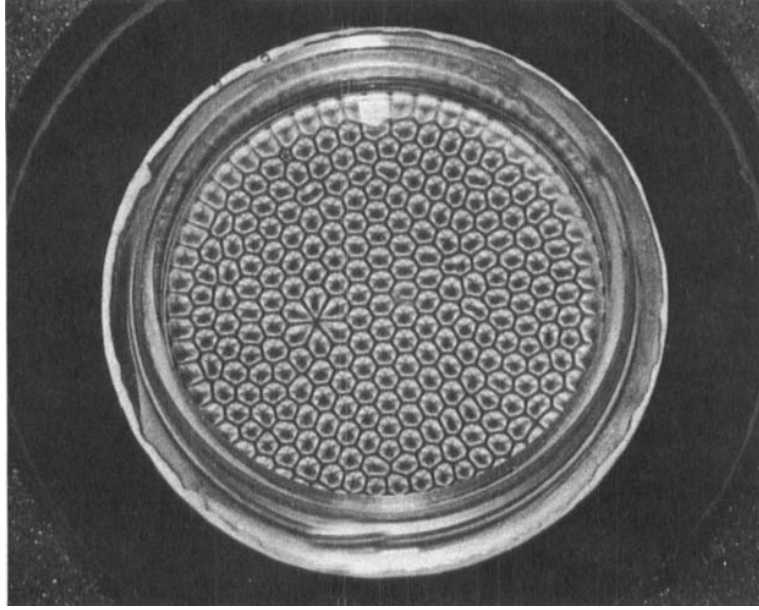


Figure 1: Convection cells (top view) formed due to Bénard-Marangoni convection. We observe cells which are not hexagonal in nature and which locally form a star-like pattern (a dislocation). The experimental result is taken from [21] and is reprinted here with permission from Wiley (permission contract is currently in progress).

2 Governing equations: strong form

This problem represents a coupled thermal/fluid problem. The governing equations follow from conservation of mass, linear momentum and energy. For an introduction to the mathematical theory of thermally driven instabilities in fluid layers heated from below, we refer the reader to Chandrasekhar's monograph [11].

As mentioned earlier, there are two effects which may be driving the flow. Buoyancy-driven flow is a consequence of the fact that the density, ρ , is a function of the temperature, T . This gives rise to a volumetric body force in the presence of temperature gradients. Surface-tension-driven flow is due to the fact that surface tension strength, measured through the coefficient γ , is a function of the temperature, which gives rise to tangential forces along the free surface in the presence of temperature gradients. In our linearized model, the surface tension and the density both vary linearly with the temperature

$$\rho(T) = \rho_0 (1 - \beta (T - T_0)), \quad (1)$$

$$\gamma(T) = \gamma_0 (1 - \tau (T - T_0)), \quad (2)$$

where ρ_0 and γ_0 are the reference values for the density and surface tension at the temperature T_0 , while β and τ are positive constants. The reference temperature $T = T_0$ is imposed on the bottom surface. At the top surface we assume that, in the absence of convection, the temperature is held at a constant value $T = T_1$. Furthermore, we introduce Θ , the deviation of the temperature from a linear profile between $T = T_0$ at the bottom and $T = T_1$ at the top, i.e.,

$$T(\mathbf{x}, t) = T_0 - \frac{\Delta T}{d} x_3 + \Theta(\mathbf{x}, t), \quad (3)$$

where d is the height of the container and $\Delta T = T_1 - T_0$; see Figure 2.

Introducing the velocity $\mathbf{u} = (u_1, u_2, u_3)$, the pressure p , and the temperature T , the governing equations can be expressed as

$$\nabla \cdot \mathbf{u} = 0 \quad \text{in } \Omega, \quad (4)$$

$$\rho_0 \frac{D\mathbf{u}}{Dt} - \mu \nabla^2 \mathbf{u} + \nabla p = g \rho(T) \mathbf{e}_3 \quad \text{in } \Omega, \quad (5)$$

$$\rho_0 c \frac{DT}{Dt} - k \nabla^2 T = u_3 \quad \text{in } \Omega, \quad (6)$$

where g is the gravity, μ the dynamic viscosity, c the heat capacity, k the thermal conductivity, \mathbf{e}_3 the unit vector in the third direction and $\frac{D}{Dt}$ is the total derivative.

Hence, the fluid is modelled as an incompressible fluid, with a buoyancy term arising from small density variations; see (1). This is the well known Boussinesq approximation [11]. The fluid flow is also coupled to the temperature via the surface tension; see (2). The temperature is coupled to the fluid through the convection term in (6).

The domain Ω represents the fluid layer. The bottom and top surfaces of the domain are denoted by $\partial\Omega_b$ and $\partial\Omega_t$, respectively. The top surface is modelled as a flat free surface. The vertical side walls are denoted as $\partial\Omega_s$. Some sample geometries are given in Figure 2.

Boundary conditions

We assume that the bottom surface, as well as the vertical side walls, are all rigid. Hence, along $\partial\Omega_b$ and $\partial\Omega_s$ we impose homogenous Dirichlet boundary conditions for the velocity,

$$u_i = 0, \quad \text{on } \overline{\partial\Omega_b} \cup \overline{\partial\Omega_s}, \quad i = 1, 2, 3.$$

Along the top surface $\partial\Omega_t$ we impose the Marangoni boundary conditions

$$\begin{aligned} \mu \frac{\partial u_1}{\partial x_3} &= -\gamma(T) \frac{\partial T}{\partial x_1}, \\ \mu \frac{\partial u_2}{\partial x_3} &= -\gamma(T) \frac{\partial T}{\partial x_2}, \\ u_3 &= 0. \end{aligned}$$

The first two equations express continuity of the tangential stress across the free surface [39], while the last equation is consistent with the fact that the free surface is treated as flat and stationary.

The temperature is subject to the boundary conditions

$$\begin{aligned} \frac{\partial T}{\partial n} &= -\frac{\Delta T}{d} + \frac{\partial \Theta}{\partial n} && \text{on } \partial\Omega_t, \\ \frac{\partial T}{\partial n} &= 0 && \text{on } \partial\Omega_s, \\ T &= T_0 && \text{on } \partial\Omega_b, \end{aligned}$$

where $\frac{\partial}{\partial n}$ denotes the derivative in the outward normal direction.

Treatment of the pressure

Before we proceed with non-dimensionalizing the governing equations, we comment a bit more on the treatment of the pressure. In the momentum equations the buoyancy term on the right hand side can be expressed as

$$\rho_0 g \delta_{i3} (1 - \beta (T - T_0)) = \rho_0 g \delta_{i3} + \rho_0 g \delta_{i3} \beta \frac{\Delta T}{d} x_3 - \rho_0 g \delta_{i3} \beta \Theta.$$

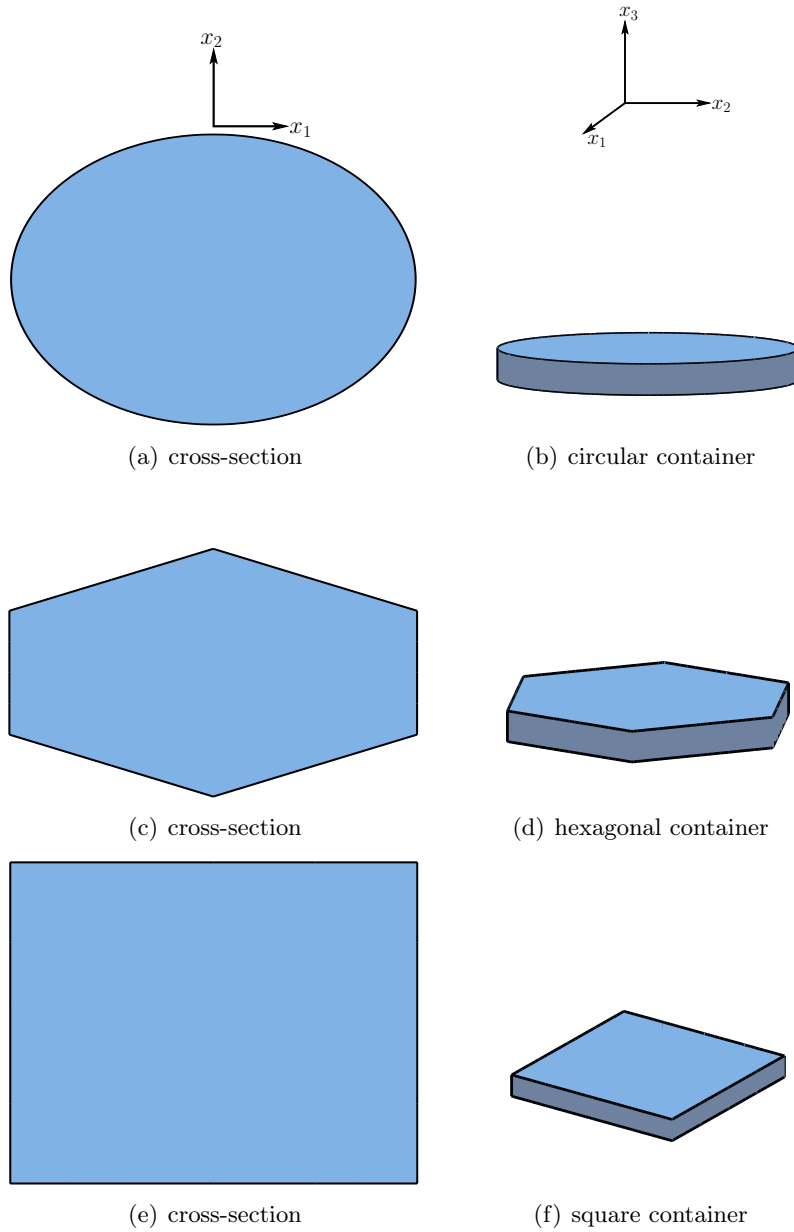


Figure 2: Some examples of the geometries we consider. The cross-sections are depicted in the left column. These are extruded to form the full 3D geometries depicted in the right column. The height of the containers is denoted by d .

The first two terms can alternatively be expressed as

$$\rho_0 g \delta_{i3} + \rho_0 g \delta_{i3} \beta \frac{\Delta T}{d} x_3 = \frac{\partial}{\partial x_3} \left(\rho_0 g x_3 + \frac{1}{2} \rho_0 g \beta \frac{\Delta T}{d} x_3^2 \right) \delta_{i3}.$$

We can thus absorb the two terms by defining a modified pressure

$$p^*(\mathbf{x}, t) = p(\mathbf{x}, t) + \rho g x_3 + \frac{1}{2} \rho_0 g \beta \frac{\Delta T}{d} x_3^2.$$

This modified pressure has a readily available physical interpretation; it simply includes the hydrostatic pressure (the term $\rho g x_3$) and the contribution from the buoyancy associated

with the linear temperature profile, $\frac{1}{2}\rho_0 g \beta \frac{\Delta T}{d} x_3^2$. In summary, we have that

$$-\frac{\partial p}{\partial x_i} + \rho_0 g \delta_{i3} (1 - \beta(T - T_0)) = -\frac{\partial p^*}{\partial x_i} + \rho_0 g \delta_{i3} \beta \Theta.$$

In the following, we drop the superscript $*$ and this modified pressure is assumed.

Non-dimensionalization

We now proceed with non-dimensionalizing the governing equations; see [41]. For the spatial coordinates a natural length scale is the height of the container

$$x'_i = x_i/d, \quad i = 1, 2, 3.$$

For time we use the thermal diffusivity time constant,

$$t' = t/(d^2/\alpha_T),$$

where the thermal diffusivity is $\alpha_T = k/(\rho_0 c)$. These two together naturally give us the velocity scale as the ratio $d/(d^2/\alpha_T) = \alpha_T/d$, and we non-dimensionalize the velocity as

$$u'_i = u_i/(\alpha_T/d), \quad i = 1, 2, 3.$$

The pressure is non-dimensionalized as

$$p' = p/(\mu \alpha_T/d^2),$$

while the temperature is scaled using the temperature difference ΔT ,

$$T' = T/\Delta T.$$

Together with (1)-(3), the chosen scales give us the governing equations on non-dimensional form:

$$\nabla \cdot \mathbf{u} = 0 \quad \text{in } \Omega, \quad (7)$$

$$\frac{1}{Pr} \frac{D\mathbf{u}}{Dt} - \nabla^2 \mathbf{u} + \nabla p = Ra \Theta \mathbf{e}_3 \quad \text{in } \Omega, \quad (8)$$

$$\frac{D\Theta}{Dt} - \nabla^2 \Theta = u_3 \quad \text{in } \Omega, \quad (9)$$

where we have dropped the primes for clarity of presentation. We have introduced the Prandtl number,

$$Pr = \frac{\nu}{\alpha_T},$$

where $\nu = \mu/\rho_0$ is the kinematic viscosity, as well as the Rayleigh number,

$$Ra = \frac{g\beta\Delta T d^3}{\alpha_T \nu}.$$

The corresponding velocity conditions on the boundary $\partial\Omega_t$ can be expressed as

$$\frac{\partial u_1}{\partial x_3} = -Ma \frac{\partial \Theta}{\partial x_1}, \quad (10)$$

$$\frac{\partial u_2}{\partial x_3} = -Ma \frac{\partial \Theta}{\partial x_2}, \quad (11)$$

$$u_3 = 0, \quad (12)$$

where Ma is the Marangoni number

$$Ma = \frac{\gamma_0 \tau \Delta T d}{\mu \alpha_T},$$

and the boundary conditions for the temperature are given as

$$\frac{\partial \Theta}{\partial n} = 0 \quad \text{on } \partial \Omega_t, \quad (13)$$

$$\frac{\partial \Theta}{\partial n} = 0 \quad \text{on } \partial \Omega_s, \quad (14)$$

$$\Theta = 0 \quad \text{on } \partial \Omega_b. \quad (15)$$

The system is thus parameterized through four non-dimensional numbers: Pr , Ra , Ma , and Γ , the aspect ratio of the container. Here,

$$\Gamma = \frac{\sqrt{A}}{d},$$

where A is the cross-sectional area and d is the height of the container.

Finally, we need to specify initial conditions for the temperature and the velocity. We will return to this shortly.

3 Governing equations: the weak form

We now present the weak formulation of the non-dimensionalized problem (7)-(9) subject to the boundary conditions (10)-(15). We introduce the function spaces X_i, Y and Z defined as

$$\begin{aligned} X_1 = X_2 &= \{v(t) \in H^1(\Omega), v(t) = 0 \text{ on } \overline{\partial \Omega_b} \cup \overline{\partial \Omega_s}\}, \\ X_3 &= \{v(t) \in H^1(\Omega), v(t) = 0 \text{ on } \overline{\partial \Omega_b} \cup \overline{\partial \Omega_s} \cup \overline{\partial \Omega_t}\}, \\ Y &= \{q \in L^2(\Omega)\}, \\ Z &= \{v(t) \in H^1(\Omega), v(t) = 0 \text{ on } \overline{\partial \Omega_b}\}. \end{aligned}$$

The governing equations for the fluid flow can then be expressed as:

Find $u_i(t) \in X_i$, $i = 1, 2, 3$, and $p(t) \in Y$ such that

$$\begin{aligned} \frac{1}{Pr} \int_{\Omega} v_i \left(\frac{\partial u_i}{\partial t} + \mathbf{u} \cdot \nabla u_i \right) d\Omega &= \\ \int_{\Omega} \left(-\nabla u_i \cdot \nabla v_i + p \frac{\partial v_i}{\partial x_i} \right) d\Omega + I_{\gamma, i}(v_i) &\quad \forall v_i \in X_i, \\ \int_{\Omega} q \nabla \cdot \mathbf{u} d\Omega &= 0 \quad \forall q \in Y, \end{aligned}$$

where *no* summation over repeated indices is assumed. Here $I_{\gamma, i}$, $i = 1, 2, 3$, represent the terms due to the Marangoni boundary conditions on $\partial \Omega_t$, as well as the buoyancy term for the third component, i.e.,

$$I_{\gamma, 1}(v_1) = -Ma \int_{\partial \Omega_t} \frac{\partial \Theta}{\partial x_1} v_1 dA, \quad (16)$$

$$I_{\gamma, 2}(v_2) = -Ma \int_{\partial \Omega_t} \frac{\partial \Theta}{\partial x_2} v_2 dA, \quad (17)$$

$$I_{\gamma, 3}(v_3) = Ra \int_{\Omega} \Theta v_3 d\Omega. \quad (18)$$

The temperature problem reads:

Find $\Theta \in Z$ such that

$$\int_{\Omega} v \left(\frac{\partial \Theta}{\partial t} + \mathbf{u} \cdot \nabla \Theta \right) d\Omega = \int_{\Omega} (-\nabla v \cdot \nabla \Theta + v u_3) d\Omega \quad \forall v \in Z.$$

4 Discretization

We now discretize the weak form of the governing equations using spectral elements [28]. The geometry is represented using isoparametric elements, i.e., within each element Ω^k , $k = 1, \dots, K$, we represent the physical coordinates using a nodal, tensor-product basis,

$$x_i^k(r_1, r_2, r_3) = \sum_{l=0}^N \sum_{m=0}^N \sum_{n=0}^N (x_i^k)_{lmn} \ell_l(r_1) \ell_m(r_2) \ell_n(r_3), \quad i = 1, 2, 3,$$

where $(x_i^k)_{lmn}$ are the basis coefficients, and $\ell_p(r) \in \mathbb{P}_N(-1, 1)$ is the one-dimensional Lagrangian interpolant through the Gauss-Lobatto Legendre points ξ_q , $q = 0, \dots, N$, with $\ell_p(\xi_q) = \delta_{pq}$. The nodes are first distributed along the edges of the elements, before we use the Gordon-Hall algorithm to generate the nodal values from the given surface values [19]. Some examples of the resulting grids used are depicted in Figure 3. The semi-discrete equations (discrete in space, continuous in time) can be stated on the form

$$\frac{1}{Pr} \left(\mathbf{B} \frac{d\mathbf{u}}{dt} + \mathbf{C}\mathbf{u} \right) + \mathbf{A}\mathbf{u} = \mathbf{D}^T p + \mathbf{I}_\gamma, \quad (19)$$

$$\mathbf{D}\mathbf{u} = \mathbf{0}, \quad (20)$$

$$\mathbf{B} \frac{d\Theta}{dt} + \mathbf{C}\Theta = -\mathbf{A}\Theta + \mathbf{B}u_3, \quad (21)$$

where \mathbf{A} denotes the discrete Laplacian and \mathbf{B} the velocity mass matrix. Note that these operators are vector operators; in particular they impose different boundary conditions on the different velocity components. Furthermore, \mathbf{C} denotes the discrete (nonlinear) convection operator, \mathbf{D} the discrete divergence operator and \mathbf{D}^T the discrete gradient operator. Finally, \mathbf{I}_γ is the discrete realization of the integrals given in (16)-(18).

The semi-discrete equations are now discretized in time using the backward difference method [18]. A pressure-correction projection scheme is used to split the velocity and pressure in the momentum equations [42, 20, 40]. The convection is handled through an operator-integrating-factor (OIF) scheme [29]. In the simulations presented later we have used a second order temporal scheme, however, for clarity of presentation we here present the discrete equations for a first order temporal realization [5]. At each time level we start by solving three convection problems, one for each velocity component. This consists of integrating the semi-discrete convection equations

$$\begin{aligned} \frac{d\tilde{u}_i}{d\tau} &= -\mathbf{B}^{-1} \mathbf{C}(\mathbf{u}^*) \tilde{u}_i, \\ \tilde{u}_i(0) &= u_i^n, \quad i = 1, 2, 3, \end{aligned}$$

from $\tau = 0$ to $\tau = \Delta t$ using the classical 4th order explicit Runge-Kutta (RK4) scheme [18]. The convecting velocity field \mathbf{u}^* represents an extrapolant for the velocity in (t^n, t^{n+1}) ; for a first order realization we simply use

$$\mathbf{u}^* = \mathbf{u}^n.$$

We need this extrapolant when integrating the three convection problems as we need values for the velocity between $\tau = 0$ and $\tau = \Delta t$ which are not available to us at this point in time. For a first or a second order realization, a zeroth, respectively first, order extrapolant retain the full temporal order of the overall scheme. This is an application of the OIF-scheme and the calculation allows us to approximate the total derivative at time level t^{n+1} . We denote the output from this calculation by $\tilde{\mathbf{u}}^{n+1}$.

With the convection problems solved, we can move on to solving the momentum equations. As mentioned earlier we use a velocity-pressure splitting scheme; in particular, the equations for the velocity is decoupled from the pressure by using an extrapolant for the pressure which we denote by p^* . Again, the order of this extrapolant is taken as one less than the temporal order of the overall scheme. This gives us the following equations for the velocity,

$$\mathbf{H}\hat{\mathbf{u}}^{n+1} = \frac{1}{Pr\Delta t}\mathbf{B}\tilde{\mathbf{u}}^{n+1} + \mathbf{D}^T p^* + \mathbf{I}_\gamma,$$

where p^* is the pressure extrapolant as discussed earlier, and $\mathbf{H} = \mathbf{A} + \frac{1}{\Delta t}\mathbf{B}$ is the discrete Helmholtz operator.

The third step in the solution of the momentum equations is correcting the velocity by projecting it onto the space of divergence-free fields. In practice, this is done through solving an elliptic problem for the pressure,

$$\mathbf{E}\Delta p = -\frac{1}{Pr\Delta t}\mathbf{D}\hat{\mathbf{u}}^{n+1},$$

where $\mathbf{E} = \mathbf{D}\mathbf{B}^{-1}\mathbf{D}^T$ is the consistent pressure Poisson operator. We then update the pressure and the velocity through

$$\begin{aligned} p^{n+1} &= p^* + \Delta p, \\ \mathbf{u}^{n+1} &= \hat{\mathbf{u}}^{n+1} + Pr\Delta t\mathbf{B}^{-1}\mathbf{D}^T\Delta p. \end{aligned}$$

The final problem to be solved is the energy equation. Again, we start by solving a convection problem,

$$\begin{aligned} \frac{d\tilde{\Theta}}{d\tau} &= -\mathbf{B}^{-1}\mathbf{C}(\mathbf{u}^*)\tilde{\Theta}, \\ \tilde{\Theta}(0) &= \Theta^n, \end{aligned}$$

from $\tau = 0$ to $\tau = \Delta t$ using RK4. The output of this calculation is denoted as $\tilde{\Theta}^{n+1}$.

With the convection step completed, we can solve the elliptic temperature problem resulting from the convection-diffusion equation expressed in a Lagrangian framework,

$$\mathbf{H}\Theta^{n+1} = \mathbf{B}\left(u_3^{n+1} + \frac{1}{\Delta t}\tilde{\Theta}^{n+1}\right).$$

Note that the operators \mathbf{H} and \mathbf{B} are not identical to those considered for the fluid problem; they are here associated with the scalar temperature field, and temperature boundary conditions are imposed.

At this point we have arrived at new values for the velocity, the pressure and the temperature at time level t^{n+1} ; the solution is advanced forward in time by repeating this overall procedure.

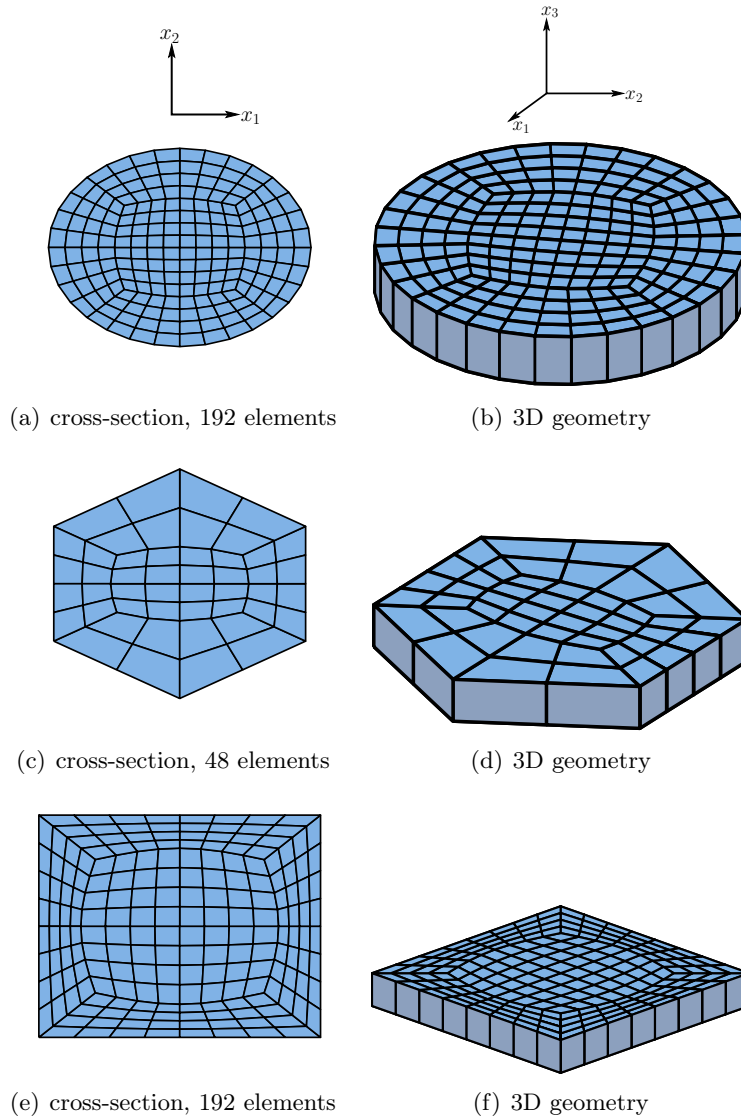


Figure 3: Some examples of the grids we consider. The cross-sections with their elemental decomposition are given in the left column. As can be seen in the right column, we here only consider a single layer of spectral elements in the vertical direction.

Initial conditions

As previously mentioned, we need to supply the system with initial conditions for the velocity and temperature. For the velocity we simply start with all components exactly equal to zero, i.e.,

$$u_1^0 = u_2^0 = u_3^0 = 0.$$

For the temperature we usually start by calculating a random field in the x_1x_2 plane, hereby denoted by $Rand(x_1, x_2)$. We then multiply this field by a suitable function in the third direction. This procedure gives the initial condition

$$\theta^0(x_1, x_2, x_3) = Rand(x_1, x_2)x_3(2 - x_3).$$

The function $x_3(2 - x_3)$ is chosen since it is compatible with the boundary conditions in the third direction, namely

$$\begin{aligned}\theta(x_1, x_2, 0) &= 0, \\ \frac{\partial \theta}{\partial x_3}(x_1, x_2, 1) &= 0.\end{aligned}$$

This initial condition was also used in [30].

Equation solvers

The geometries we consider are of a particular kind; see Figures 2 and 3. Specifically, all cross-sections are invariant in the third direction. This allows us to use the algorithms developed in [26, 27, 4]. These are specialized algorithms which exploit the tensor-product structure available in these geometries and these grids, saving us close to an order of magnitude in computational time compared to not exploiting this feature. In addition, all our numerical results have been obtained through parallel processing using a combined MPI/OpenMP implementation [26].

5 Verification

We now perform several tests to confirm that our simulation tool behaves as expected.

Analytic solution and data

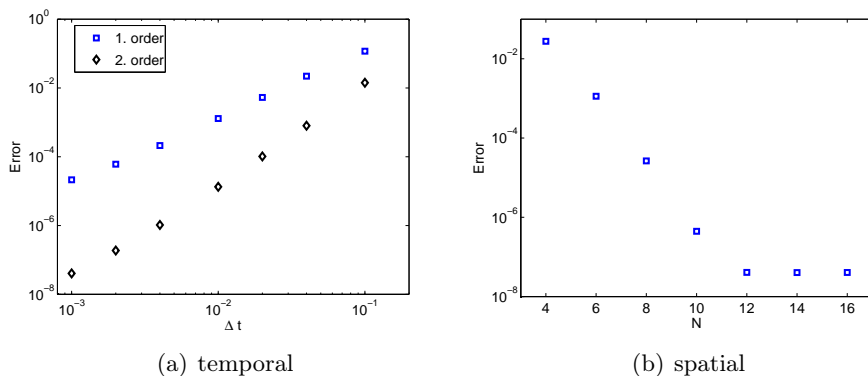


Figure 4: The left plot depicts the discretization error of the velocity measured in the discrete H^1 -norm at time $t = 1$ as a function of the time step, Δt , for a first and second order temporal splitting scheme; here, $K = 48$ spectral elements are used, each of order $N = 16$. We observe the expected first and second order convergence. The right plot depicts the same error as a function of the polynomial degree, N , for a fixed time step and a fixed number of elements. We observe the expected exponential convergence. The temporal error is here subdominant for $N < 12$.

First, we solve the three-dimensional Navier-Stokes equations in a cylindrical domain $0 \leq r \leq R$, $0 \leq z \leq d$. We use a forcing function compatible with the known analytical solution

(here expressed in cylindrical coordinates)

$$\begin{aligned}
u_r(r, \theta, z, t) &= \frac{1}{5} \sin^2(\pi r) \sin(\theta) \sin(2\pi z) \sin t, \\
u_\theta(r, \theta, z, t) &= -\frac{1}{5} \sin^2(\pi r) \cos(\theta) \sin(2\pi z) \sin t, \\
u_z(r, \theta, z, t) &= \frac{1}{10\pi} \sin(\pi r) \left(2\pi \cos(\pi r) + \frac{2}{r} \sin(\pi r) \right) \sin(\theta) (\cos(2\pi z) - 1) \sin t, \\
p(r, \theta, z, t) &= \sin^2(\pi r) \sin(\pi z) \sin t.
\end{aligned}$$

The difference between the exact and numerical solution is measured in the discrete H^1 -norm. The convergence results in Figure 4 show the expected behavior: first and second order convergence in time, as well as exponential convergence in space for problems with analytic solutions and data.

Verification in a periodic geometry

Here, we follow the example from [39]. We assume an infinite Prandtl number and a zero Rayleigh number. At steady state this corresponds to the limit of solving the steady Stokes equations under zero gravity conditions. Hence, we do not have an evolution equation for the momentum, and we resort to a Uzawa decoupling approach [1] to handle the momentum equations at each time level. Note that, even though the velocity do not follow an evolution equation directly, the velocity field will not be constant in time until we reach a steady state for the temperature field. This is because the two fields are coupled through the Marangoni boundary conditions on the top of the domain. The computational domain is given by $\Omega = (0, l_x) \times (0, l_y) \times (0, d)$ where

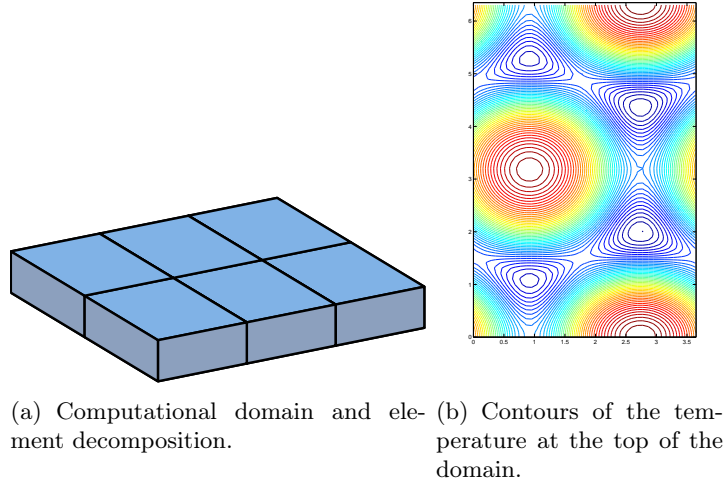
$$\frac{l_x}{d} = \frac{4\pi}{\sqrt{3}k}, \quad \frac{l_y}{d} = \frac{4\pi}{k},$$

with $k = 1.9929$. Periodic boundary conditions are specified along $\partial\Omega_s$. The specified periodicity lengths are compatible with the formation of a single hexagonal cell as predicted by linear stability theory; [11, 22, 32].

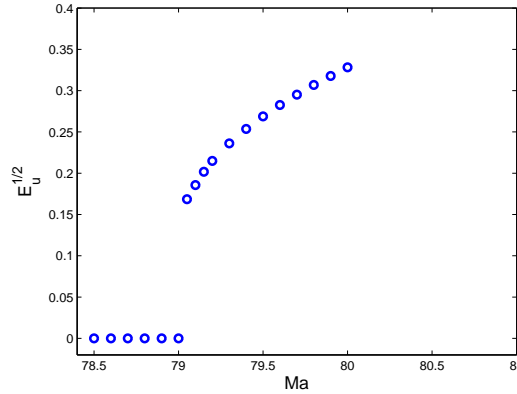
As our indicator we use the kinetic energy,

$$E_u = \frac{1}{V} \int_{\Omega} (u_1^2 + u_2^2 + u_3^2) \, d\Omega,$$

where V is the volume of Ω . The main purpose of this test is to determine the critical Marangoni number. We first do a calculation for $Ma = 100$, which is well above the published critical value. Next, we take the fields we obtain at steady state for this calculation as initial conditions for new simulations where the Marangoni number is lowered. We then observe for which Marangoni number the flow vanishes. Linear stability theory predicts that the critical Marangoni number should be $Ma_c = 79.6$, but that in the a subcritical regime $Ma \in (79.15, 79.6)$, the hexagonal cells should prevail [8, 36]. The results given in Figure 5 show that our obtained values are in good agreement with those obtained in earlier numerical experiments [39], as well as those predicted by linear stability theory [8, 36].



(a) Computational domain and element decomposition. (b) Contours of the temperature at the top of the domain.



(c) Energy plot.

Figure 5: A plot of the energy measure $E_u^{1/2}$ at steady state for different values of the Marangoni number. The obtained values are in good agreement with previously reported results.

Establishing grid independence

For the fully coupled fluid/temperature problem with rigid walls, we do not have any quantitative data to compare against, i.e., we cannot do convergence tests to establish correctness of the code. However, a necessary requirement is that we obtain a grid-independent solution once all the spatial and temporal features of the solution are resolved.

As a test case we consider a circular container with an aspect ratio $\Gamma = 8.38$. The value of Γ is chosen slightly above the value which yields a seven cell solution according to [30]. We use a Marangoni number $Ma = 105$ in order to be sure that we are well above the critical value. The Rayleigh number $Ra = 48$ and the Prandtl number $Pr = 890$.

Inspired by [30], we consider four metrics for our results. The first is simply the maximum pointwise temperature in the cylinder

$$\theta_{max} = \max_{jkl} \Theta_{jkl}.$$

The second is the kinetic energy, E_u , defined earlier, while the third is the “thermal energy”

$$E_\theta = \frac{1}{V} \int_{\Omega} \theta^2 \, d\Omega,$$

where V is the volume of Ω . The final measure is the scaled Nussel number

$$\mathcal{N}u = \frac{1}{A} \int_{\partial\Omega_t} \theta_t \, dA,$$

where θ_t denotes the temperature on the top of the domain.

We integrate the governing equations until a fixed time $t_f = 30$. This should be sufficient as the steady state pattern is formed around $t_f = 10$. The numerical results are given in Table 1.

This seems to confirm grid independence of the solution, as well as a tolerance of 10^{-6} being sufficient. However, an interesting observation is that this is only one of the final states we have obtained for the same problem. For two of the calculations we also obtained an eight cell solution (see Figure 8(b)) instead of a seven cell solution (see Figure 8(a)). The results for these two cases are given in Table 2.

Table 1: Different measures of the seven cell final state (Figure 8(a)). We consider three different grids and three different tolerances; the same tolerance is used in both the Helmholtz solver and the consistent pressure Poisson solver. Each simulation is started with a different random initial condition for the temperature. The time step is $\Delta t = \frac{1}{200}$.

tolerance	grid	θ_{\max}	$(E_u)^{\frac{1}{2}}$	$(E_\theta)^{\frac{1}{2}}$	$\mathcal{N}u$
10^{-6}	$N = 8, K = 48$	0.3128	1.9357	0.1093	0.0881
	$N = 12, K = 48$	0.3128	1.9357	0.1093	0.0881
	$N = 8, K = 192$	0.3128	1.9358	0.1093	0.0881
10^{-8}	$N = 8, K = 48$	0.3128	1.9358	0.1093	0.0881
	$N = 12, K = 48$	0.3127	1.9358	0.1093	0.0881
	$N = 8, K = 192$	0.3128	1.9358	0.1093	0.0881
10^{-10}	$N = 8, K = 48$	0.3128	1.9357	0.1093	0.0881
	$N = 12, K = 48$	0.3127	1.9358	0.1093	0.0881
	$N = 8, K = 192$	0.3128	1.9358	0.1093	0.0881

Table 2: Measures for the two simulations that yielded an eight cell solution (Figure 8(b)).

tolerance	grid	θ_{\max}	$(E_u)^{\frac{1}{2}}$	$(E_\theta)^{\frac{1}{2}}$	$\mathcal{N}u$
10^{-8}	$N = 8, K = 48$	0.3060	1.9557	0.1096	0.0901
10^{-10}	$N = 8, K = 192$	0.3061	1.9558	0.1096	0.0901

Again, it seems that the measures are sufficiently grid independent. In addition, these tests seem to indicate that, for this geometry and for the chosen non-dimensional numbers, there exist more than one final state. We will return to this issue later.

To check that the temporal component of the error also behaves as expected, we perform the same integration using a time step half the size used in Table 1. The results are given in Table 3. We seem to have about four digits of accuracy in the first calculations, something which fits nicely with the experience from convergence tests for the Navier-Stokes case. We conclude that the numerical solution also seems to behave as expected with respect to the temporal integration.

Table 3: Measures using two different time steps. We have here used $K = 48$, $N = 12$, and a tolerance $tol = 10^{-10}$.

Δt	θ_{\max}	$(E_u)^{\frac{1}{2}}$	$(E_\theta)^{\frac{1}{2}}$	Nu
$\frac{1}{200}$	0.3128	1.9357	0.1093	0.0881
$\frac{1}{400}$	0.3128	1.9358	0.1094	0.0882

Secondary instability

As mentioned in the Introduction, a secondary instability in the system has been found, both experimentally [31] as well as in a DNS [3]. As another indication of the correctness of our computational tool, we want to make sure that we can recreate this effect.

The secondary instability is known to kick in for

$$\epsilon = \frac{\Delta T - \Delta T_c}{\Delta T_c} = \frac{\Delta T}{\Delta T_c} - 1 \sim 3,$$

where ΔT_c is the critical temperature difference for convection to occur and ΔT the actual temperature difference in the system. Since the Marangoni number is linear in the temperature difference, we have to increase the Marangoni number with approximately a factor of 4. We do not know the critical Marangoni number / critical temperature difference precisely. However linear stability theory for a system without walls predicts that the critical Marangoni number lies somewhere around 79.6. The existence of walls increases this somewhat. Taking these facts into consideration, we have chosen a Marangoni number $Ma_1 = 105$ for the calculations within the primary instability regime, and a Marangoni number $Ma_2 = 400$ for the calculations within the secondary instability regime. As the cells should be square in shape [31], we have focused our attention on square containers since they should give the most uniform patterns. The results obtained for two different geometries are given in Figure 6 and Figure 7. We clearly observe that the increased Marangoni number has driven the cells toward a square shape, as predicted.

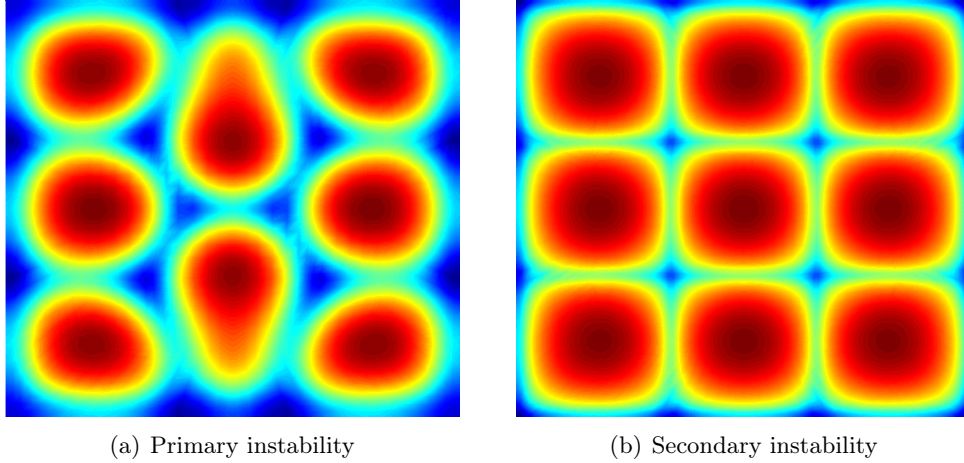


Figure 6: Two different resulting flow patterns in a square container with $\Gamma = 9.5$, $Ra = 48$, and $Pr = 890$. The left plot shows a calculation with $Ma = 105$ which is within the primary instability regime. The right plot shows a calculation with $Ma = 400$, where a secondary instability, which tends to drive the flow towards square cells, is dominating.

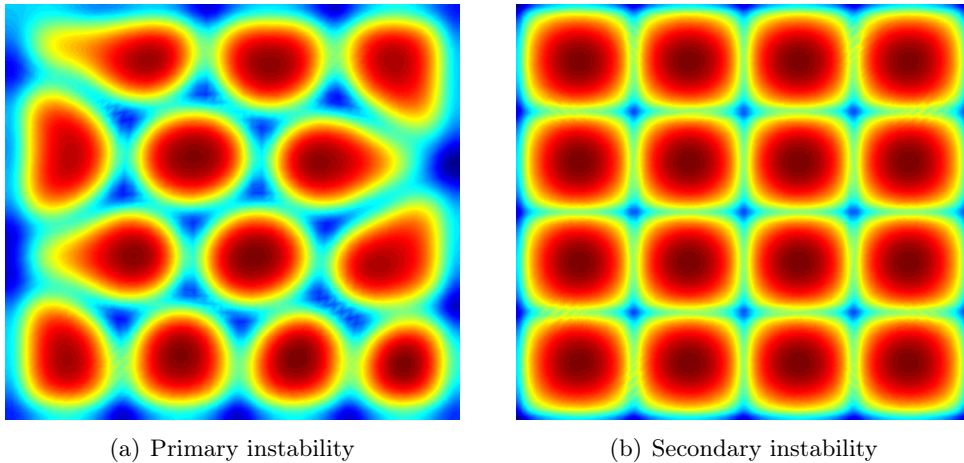


Figure 7: Two different resulting flow patterns in a square container with $\Gamma = 12.0$, $Ra = 48$, and $Pr = 890$. The left plot shows a calculation with $Ma = 105$ which is within the primary instability regime. The right plot shows a calculation with $Ma = 400$, where a secondary instability, which tends to drive the flow towards square cells, is dominating.

6 Pattern selection from random initial conditions

Since the parameter space for this problem is quite large, we have focused our attention mainly on the parameter Γ , the global aspect ratio of the computational domain, and the effect of the shape of the vessel. In these tests we start each simulation with a random initial condition for the temperature as described earlier. The majority of the simulations have been performed with $Ra = 48$ and $Ma = 105$. These values were chosen since they

are well above the critical numbers for our problems, yet well below the supercritical regime where the secondary instability (which shifts the pattern selection toward square cells) is expected to dominate. In addition, the availability of experimental data for these values is quite extensive. All simulations have been performed with $Pr = 890$ which corresponds to silicon oil. This is also the fluid used in many experiments.

We start by considering a container with a circular cross-section and $\Gamma = 8.38$. Our earlier grid independence study revealed the presence of more than one final state, and we will now investigate this effect in more detail. To this end, we perform a statistical study comprising 500 simulations, each starting from a different random initial condition for the temperature. The results are reported in Table 4.

These results indicate the importance of the initial conditions on the resulting pattern. While the seven cell pattern seems to be the preferred one (in the sense that the system selects it in the vast majority of simulations), there are several possible final states. In just 500 simulations, we observe three possible patterns for a fairly small container. We conclude that it is the random initial condition for the temperature which causes the different patterns since it is the only thing that differs between the simulations.

Table 4: Numerical results for a circular container with $\Gamma = 8.38$. The non-dimensional numbers are kept at $Ra = 48$ and $Ma = 105$. We report the number of cells observed at steady state for 500 independent calculations.

No. of cells	No. of cases
6	1
7	480
8	19

Our next series of tests involves a hexagonal container with $\Gamma = 22$. The large aspect ratio yields convection patterns with more cells, and each simulation is much more time consuming to integrate until a steady state. Again, we perform many simulations of the same system, each starting with a different random initial condition for the temperature. Most of the simulations ended up in a stationary and very regular pattern with 48 cells. However, we also found several exceptions.

The first exception is a simulation which ended up in a 52-cell pattern; see Figure 9. The second exception is a simulation which ended up in a final state with one of the cells maintained in a steady periodic (oscillatory) state which was maintained for close to a thousand units of dimensionless time; see Figure 10.

Of particular interest, however, are two patterns which ended up with a star defect resembling those observed in experiments; see Figure 1 for an experimental result and Figure 12 for our numerical results. Note that the experimental result in Figure 1 was obtained in a larger container with a circular cross-section, while our results have been obtained in a container with a hexagonal cross-section. After each defect appeared, we integrated the system for a long time and the pattern did not change, indicating that this pattern indeed represents a possible configuration of the system. It is interesting to note that we are able to obtain such a dislocation simply through a change of the initial condition. It has earlier been speculated that such defects are due to impurities in the experimental setup.

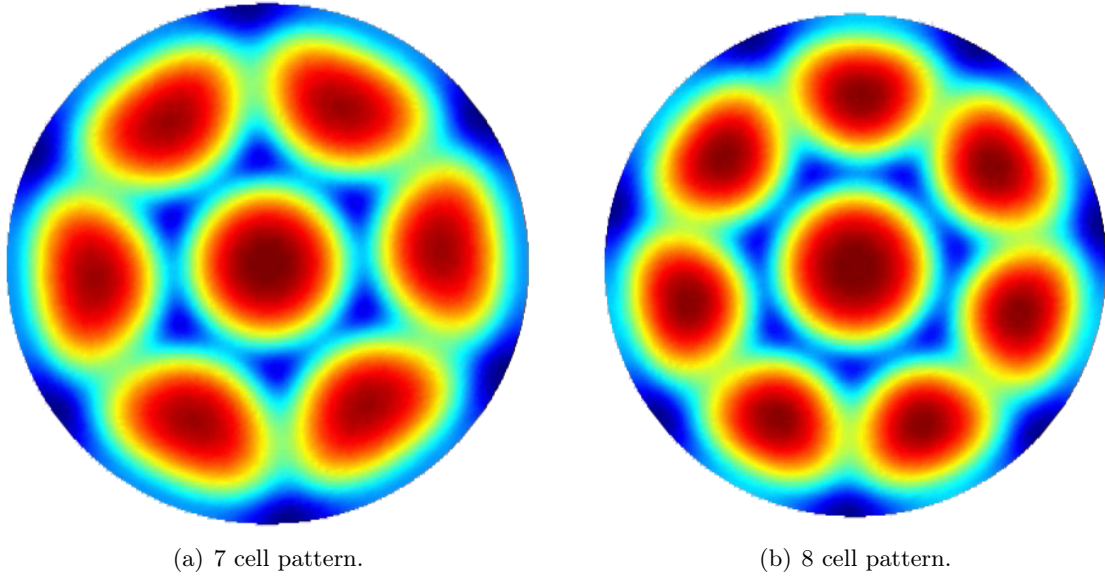


Figure 8: Two possible cell patterns obtained at steady state for $Ma = 105$, $Ra = 48$, $Pr = 890$, and $\Gamma = 8.38$.

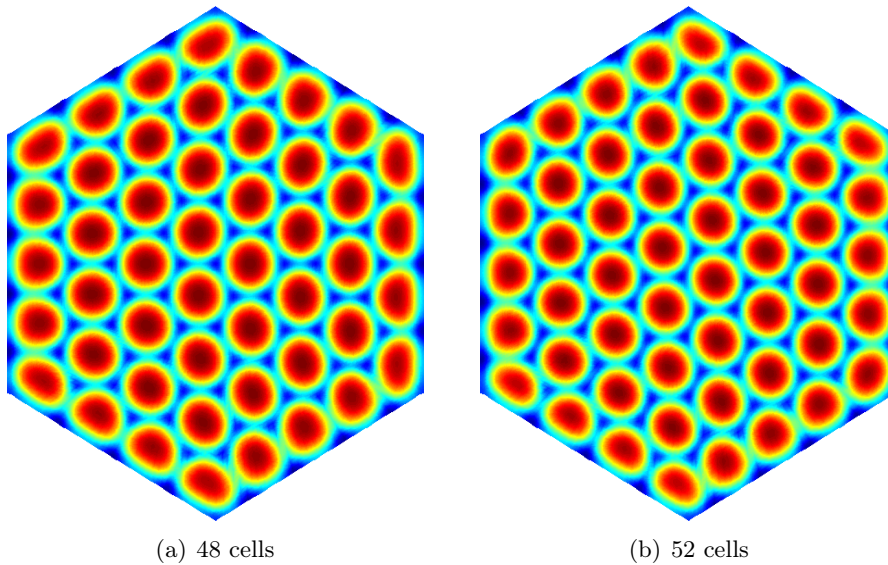


Figure 9: Two different resulting flow patterns in a hexagonal container with $Ma = 105$, $Ra = 48$, $Pr = 890$, and $\Gamma = 22$. The only difference between the two simulations is the random initial condition for the temperature. The 48-cell configuration appears to be the most common, while the 52-cell configuration is a more exceptional case.

However, our numerical result show that such defects may appear even if the geometry is perfect. Since we are only able to check a limited number of cases, it is difficult to give a precise estimate for the probability of such defects to occur. In our experiments we observed patterns with defects in 2 out of 250 simulations. Note that while the orientation

of the two patterns are different, we believe they describe the same solution. By rotating and flipping around the y -axis, we can orientate the rightmost flow pattern the same way as the leftmost. The flow patterns then look similar to the naked eye; in fact, we found a maximum pointwise error of less than 1%, measured relative to the maximum temperature. This strongly suggests that the two solutions with dislocations represent a single possible state the system can settle in (save for rotation and mirroring).

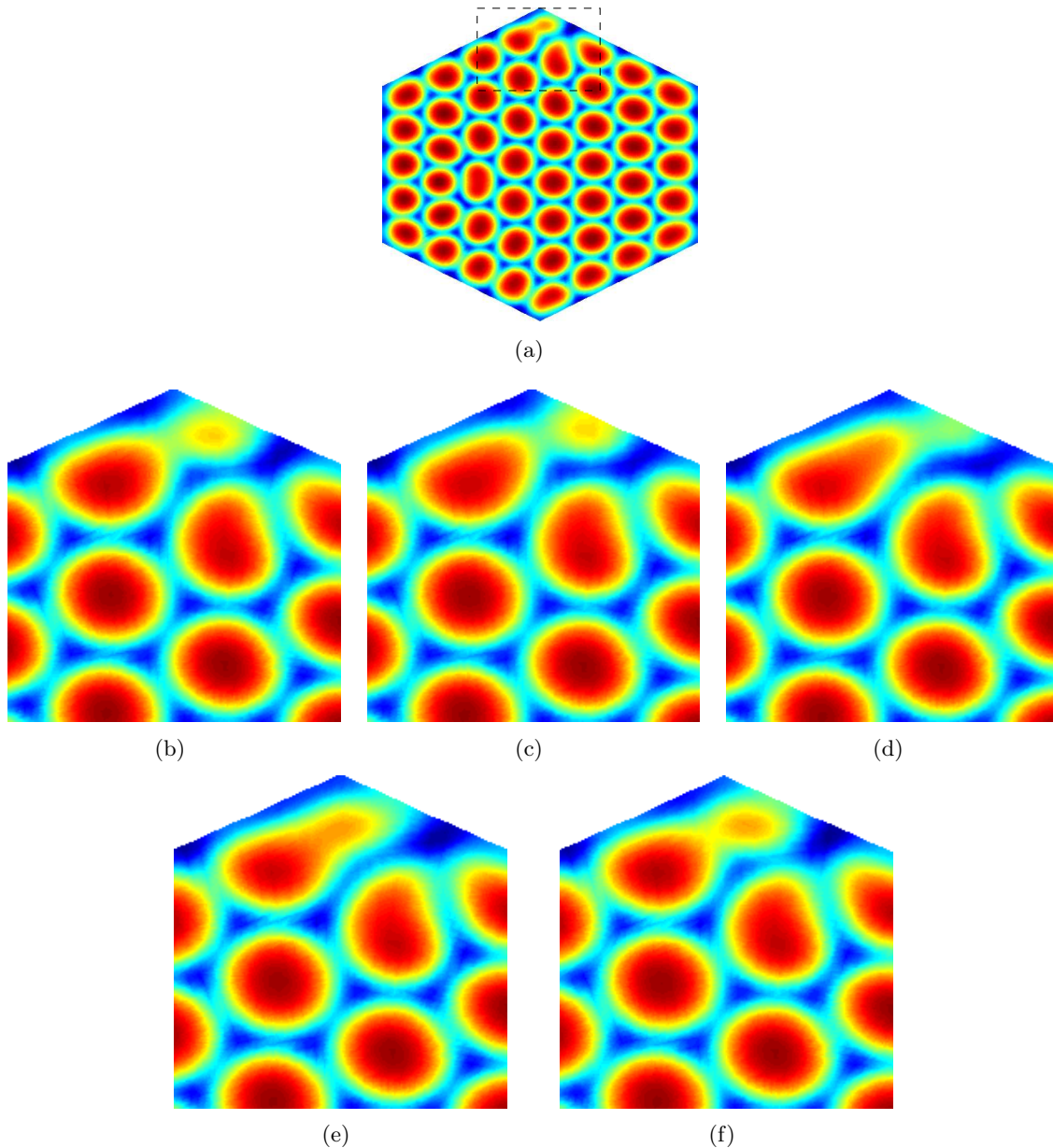


Figure 10: Final oscillatory pattern after long time integration for a hexagonal container with $Ma = 105$, $Ra = 48$, $Pr = 890$, and $\Gamma = 22$. The overall pattern is shown in (a), while the remaining plots show a close-up of the pattern near the oscillatory cell at different times during one period.

We also mention that we have performed similar tests with other containers, in which case we did not observe any defects. Overall, this seems to indicate that the appearance

of such defects is rather rare. This also fits well with the experiences from experiments where the appearance of such defects tend to be an exception rather than the norm.

The Bénard-Marangoni problem we have studied has a rich set of solutions. For the chosen Marangoni number, Rayleigh number, and Prandtl number, the key sources behind the different patterns we observe are the initial condition for the temperature and the domain aspect ratio. The importance of the initial conditions seems to grow with the aspect ratio which is only to be expected — the more cells in the pattern the larger the set of possible orientations of those cells. We have also investigated the effect of the shape of the container on the resulting patterns. In Figure 11 we give the number of cells in the final patterns for the three container shapes we have considered. We remark that some of the simulations yield a steady periodic (oscillatory) state for one or more cells after long time integration. In these cases we have taken the number of cells to be the largest number achieved during the oscillations. Our results indicate that the number of cells is fairly invariant with respect to the shape of the container.

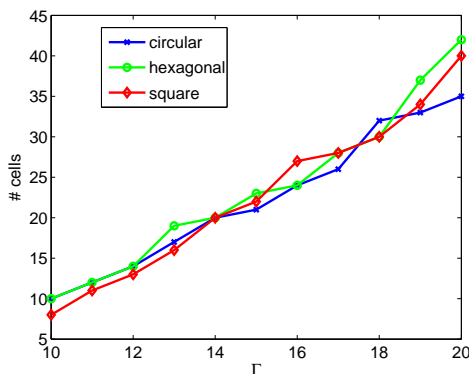


Figure 11: The number of cells in the final pattern as a function of Γ , the global aspect ratio of the domain, for circular, hexagonal and square containers. As expected, the number of cells seems to scale approximately quadratically with Γ .

Symmetrizing the initial conditions

In all the tests we have considered so far we have started with random initial conditions for the temperature; this should allow the system to select the most likely final pattern. It is also of interest to see if we are able to force the system into selecting different patterns. To this end, we perform selected tests where we impose initial conditions with inherent symmetries. We limit our attention to square and circular geometries. We choose the initial condition for the temperature with either quadrant or octant symmetry, while still being random within each quadrant/octant. In the vast majority of these tests, the enforced symmetries eventually broke down, and the system reconfigured itself into a pattern which did not exhibit the initially enforced symmetries. However, even though the initially enforced symmetry breaks down, the steady state pattern still appears to be influenced by the initial condition. In our computations the system often ended up in a pattern that differed from what we obtained if we started the system from random initial conditions without any symmetries enforced. An example of such a situation can be found in Figure 13. This might seem to contradict the findings in [9], where they found no statistically significant influence of seeding the initial condition with various patterns (triangular, square, hexagonal). However, we believe this is not the case. In experiments there will inevitably

be asymmetries introduced due to imperfections, and these asymmetries are what makes the system reconfigure itself. However, under the more “ideal” conditions offered by our numerical simulations, we also see breakdown of the initial symmetries imposed, but are able to influence the pattern selection statistics. Whether or not this is only valid in a finite time frame is an issue we have not been able to fully resolve through our computations. In the literature, experiments have been reported to have been running for days before the system eventually reconfigured itself [9]. Running such long simulations is outside the scope of our current implementation. While the breakdown of the initially imposed symmetries seems to be a general trend, we have observed exceptions. Figure 14 shows a rare case where a pattern compatible with the enforced octagonal symmetry seems to exist. If we use a slightly larger or slightly smaller container, the octagonal symmetry does break down, another indication that such configurations are highly unstable and that they are only maintainable for very specific container sizes (i.e., specific values of Γ). In Table 6 we report results where we have performed 500 simulations for the specific case $\Gamma = 8.5$, with and without enforced symmetries. In Table 5 we have performed the same test, but using the container with global aspect-ratio 8.38 discussed earlier. For the larger container, we obtain the additional the 9 cell solution as shown earlier. However, it also seems that the occurrence of the 8 cell solution has increased somewhat. These are strong indications that symmetries in the initial condition do in fact influence the pattern formation.

Table 5: Numerical results for a circular container with $\Gamma = 8.38$. The non-dimensional numbers are kept at $Ma = 105$, $Ra = 48$, $Pr = 890$. We report the number of cells observed at steady state for 500 independent simulations where we start with completely random calculations (second column) and initial conditions with enforced octagonal symmetries (third column).

No. of cells	Completely random	Symmetrized
7	481	480
8	19	20

Table 6: Numerical results for a circular container with $\Gamma = 8.50$. The non-dimensional numbers are kept at $Ma = 105$, $Ra = 48$, $Pr = 890$. We report the number of cells observed at steady state for 500 independent where we start with completely random calculations (second column) and initial conditions with enforced octagonal symmetries (third column).

No. of cells	Completely random	Symmetrized
7	468	424
8	32	73
9	0	3

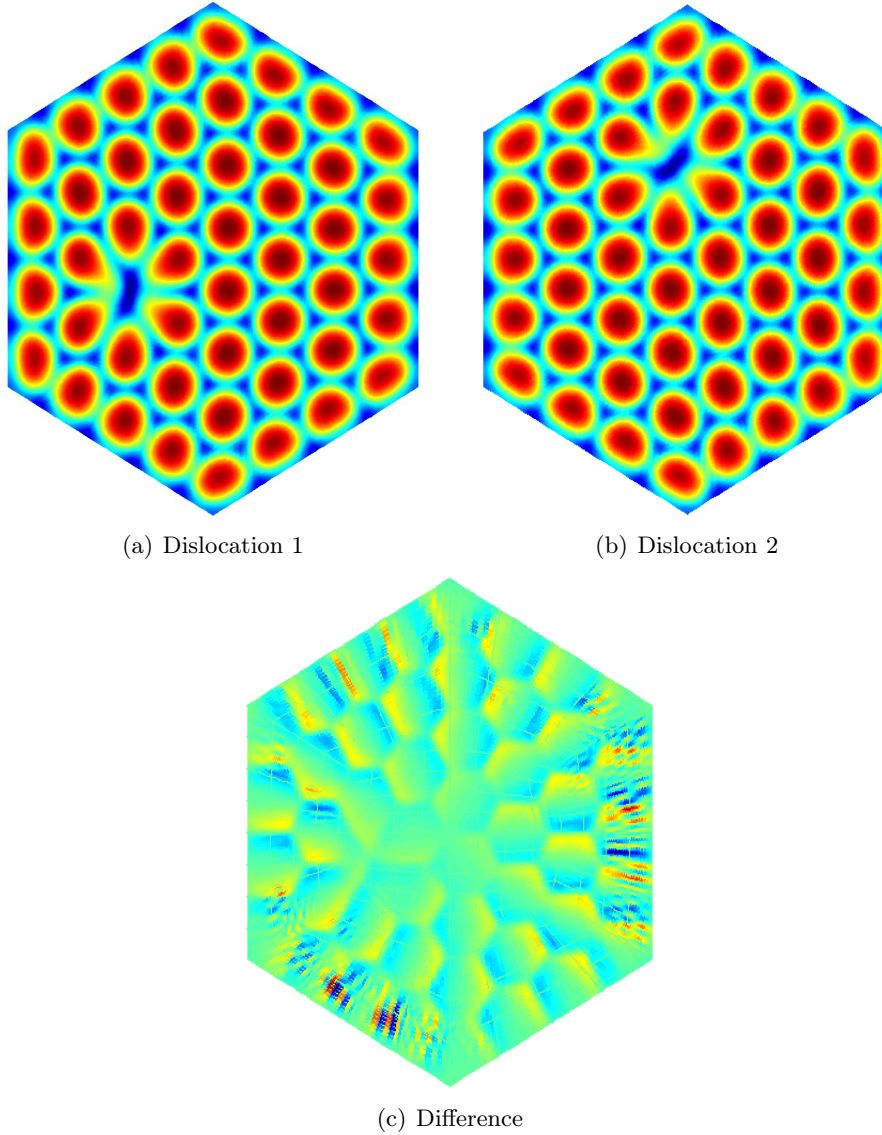


Figure 12: Two simulations which exhibit a 'star' defect resembling those which have been occasionally observed in experiments; see Figure 1. We have used $Ma = 95$, $Ra = 48$, $Pr = 890$, and $\Gamma = 22.0$. The simulations were started from random initial conditions for the temperature. The first two plots show the final patterns after long time integration, while the last plot shows the difference between the two solutions after a 90 degree rotation and then mirroring. The maximum pointwise difference between the two independent cases, measured relative to the maximum pointwise temperature, is less than 1%, indicating a fixed dislocation pattern whenever a dislocation occurs. Only two out of 200 simulations resulted in dislocations in the otherwise regular hexagonal pattern.

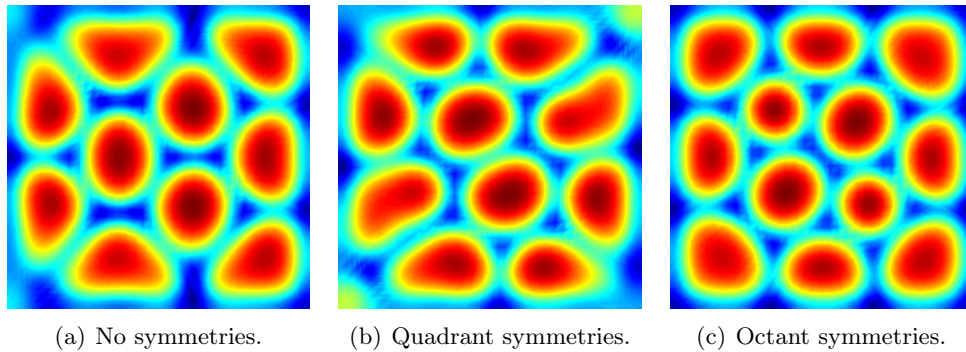


Figure 13: Resulting patterns from simulations where we enforce (a) none, (b) quadrant, or (c) octant symmetries on the initial conditions for the temperature. The final patterns are quite different, an indication that we are able to influence the pattern selection process through our choice of initial condition.

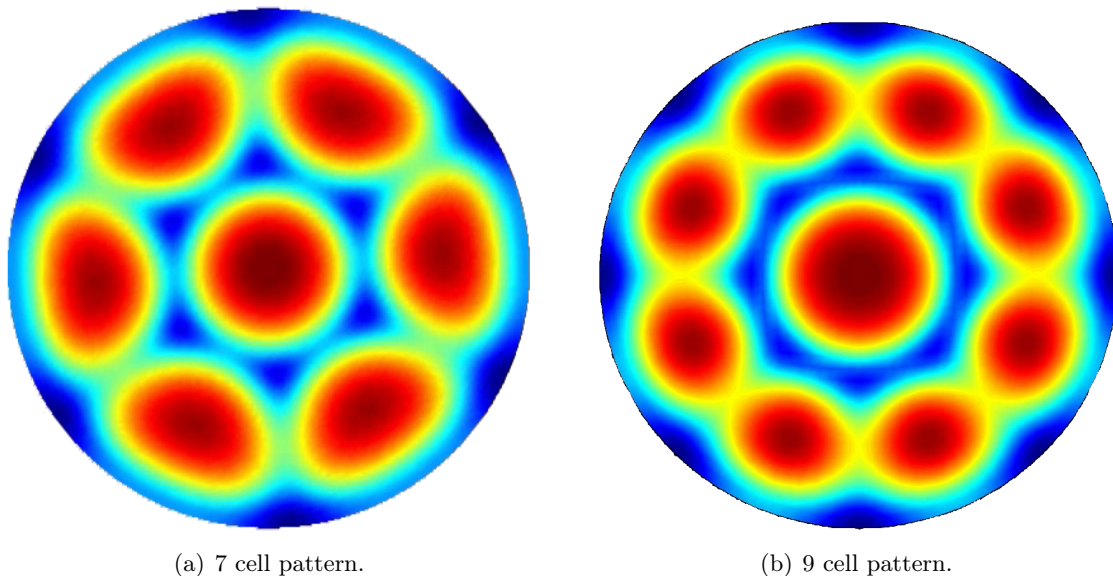


Figure 14: Steady state patterns for two simulations with $Ma = 105$, $Ra = 48$, $Pr = 890$, and $\Gamma = 8.5$. The left figure shows the pattern when we start from completely random initial conditions, while the right figure shows the pattern when we start from random initial conditions with octant symmetries. This symmetry is never broken during the simulation; the system evolves into a pattern consisting of a single cell in the middle enclosed by 8 cells around, a consequence of the original octant symmetry.

7 Results in selected deformed containers

We now turn our attention to pattern selection in slightly deformed containers. As mentioned earlier, it has been theorized [23, 21] that small geometric irregularities may have caused the (rare) dislocations observed in otherwise regular convection patterns. We will here not consider very small geometric irregularities for two reasons: (i) because of the

significant computational challenges associated with resolving small geometric details; and (ii) because our numerical results have shown that such dislocations can occur in "ideal" containers. Instead, we assume that the deformations are nontrivial and fairly regular. In the following, the deformations along the bottom surface are taken to be localized Gaussians,

$$z_0(x, y) = ae^{-\frac{(x-x_0)^2+(y-y_0)^2}{\sigma^2}}$$

where (x_0, y_0) is the center, σ the standard deviation and a the amplitude. See Figure 15 for an illustration identifying the parameters involved.

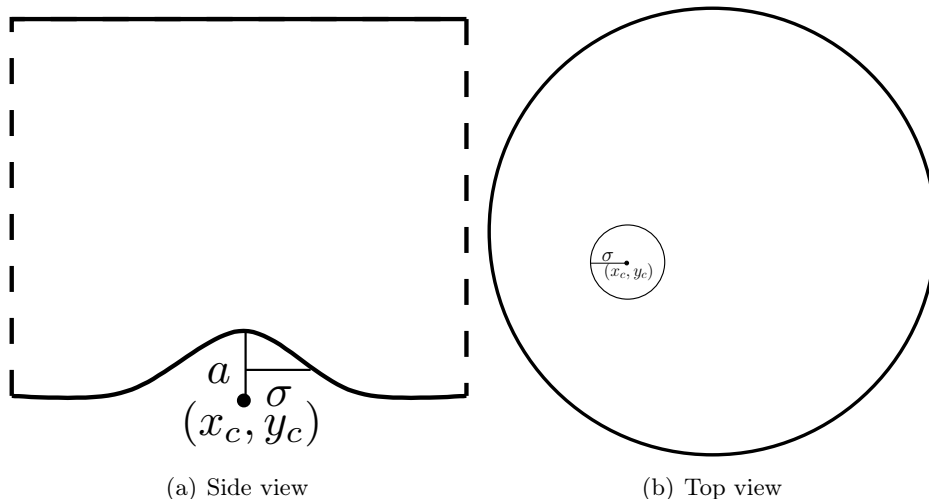


Figure 15: A cylindrical container with a Gaussian bump at the bottom. (a) Side view of the bump centered at (x_c, y_c) with standard deviation σ . We have here zoomed in on the bump to highlight the definition of the parameters. (b) Top view showing a sample placement of the bump.

In the first series of tests, we choose a deformed version of the circular container considered earlier; see Table 4 and Figure 8. We now put a small local bump with $a = 0.05$, $\sigma = 0.2$ centered at $(-2, -2)$ at the bottom. This seems to have fairly large consequences for the stability of the resulting system. While all the 100 simulations performed without the bump rapidly converged to a final stable flow pattern, most of the simulations now end up in a steady-periodic (oscillatory) state; see Table 7. With oscillatory we mean that one or more cells appear and disappear in a steady-periodic fashion; see Figure 17. However, in the cases that did settle in a steady state, we obtained the familiar (and dominant) 7 cell pattern, now slightly skewed due to the deformation on the bottom; see Figure 16. In all the cases where we obtained a steady state solution, the pattern appeared quite fast, within a few tens of non-dimensional time units and was then essentially unchanged during the rest of the simulations. In the cases where the system evolved into an oscillatory state, it stayed in this state for the rest of the simulation. It appears that the oscillatory state is a fundamental state, in the sense that, if the system evolves into such a state, it will stay oscillatory for all times.

We also performed limited tests in a larger container (the same hexagonal container discussed earlier) except this time with bumps of different sizes and amplitudes. Since these calculations take substantially longer time, we have not been able to repeat these simulations enough times to extract reliable statistical data. However, we still think some

information can be extracted from the few cases we have been able to complete.

In the first case we want to discuss, we put a bump with $a = 0.05$ and $\sigma = 2.0$ centered at $(-5, 0)$. The calculation was initialized using the 48-cell solution seen in Figure 9. The size of the bump was chosen so as to approximately cover one convection cell. The resulting pattern can be seen in Figure 18. We observe that the effect of the bump seems to be localized to the area where the bump is centered, with little or no influence on the global pattern. To see if this is a result of the particular initial condition we used, we also performed a calculation where we started from a random initial condition compatible with the deformed container. The pattern we obtained can be seen in Figure 20(a). In this case, the deformation seems to have a much larger influence on the global pattern. The pattern comes through as somewhat irregular.

In addition, one of the cells (the one at the bottom of the figure) is in a steady-periodic (oscillatory) state. Whether or not the pattern eventually will settle into something resembling Figure 18 is hard to conclude. The pattern seems quite stable; we integrated the system for about 200 units of dimensionless time before the pattern settled. We then integrated the system for another 500 units of dimensionless time without any qualitative change occurring.

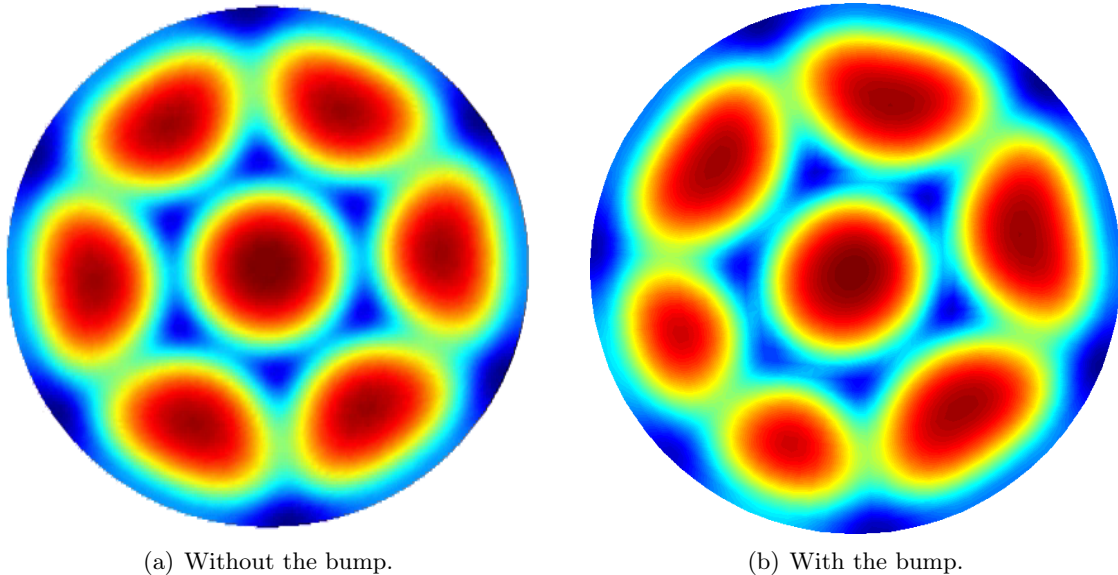


Figure 16: The resulting pattern from two computations. The left figure shows the resulting pattern in the container without the bump. The right figure shows the stationary pattern obtained when there is a bump at the bottom. The right pattern resembles the left one, except locally where the bump is placed, the system behaves as if the fluid layer is thinner.

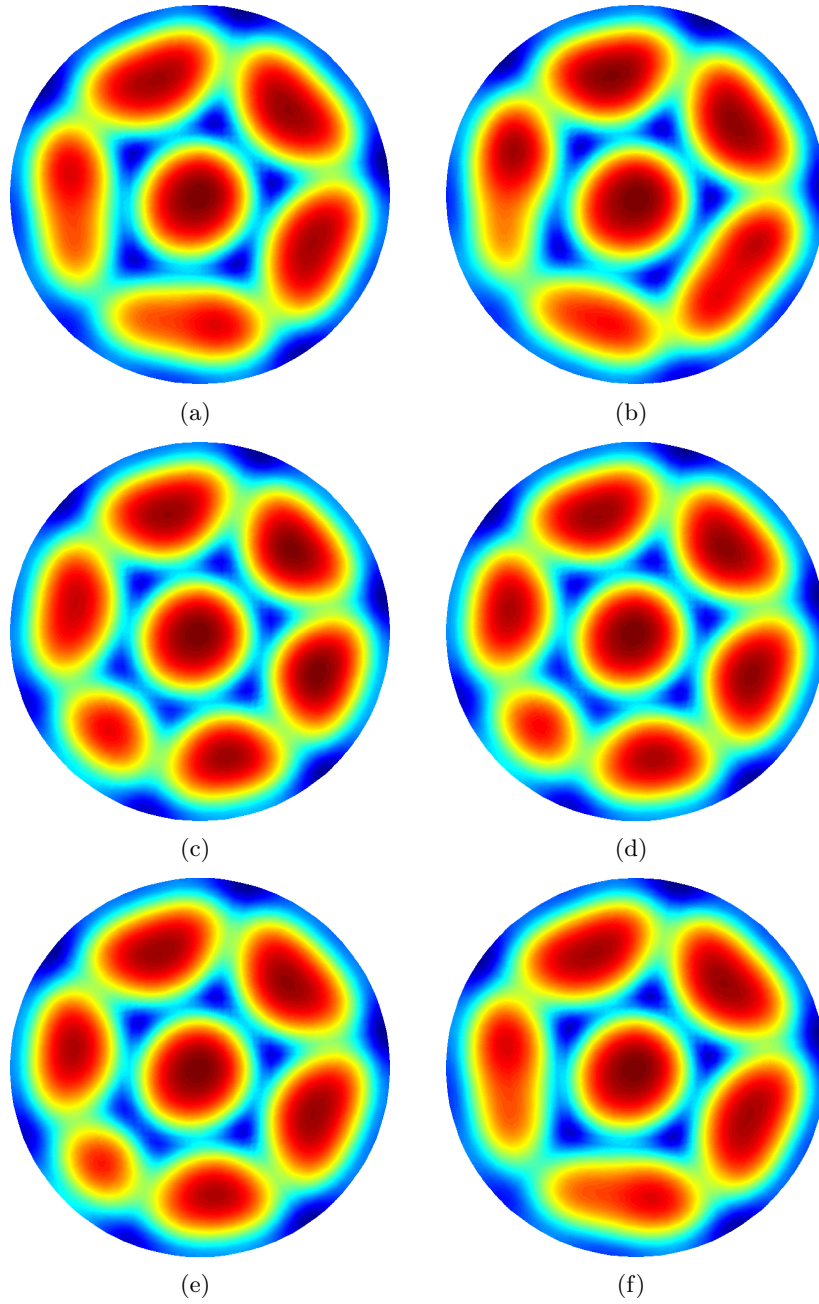


Figure 17: Final oscillatory pattern after long time integration in a circular container with $Ma = 105$, $Ra = 48$, $Pr = 890$ and $\Gamma = 8.38$. The plots show 6 evenly spaced snapshots over a single period. There is a small bump with $a = 0.05$, $\sigma = 0.2$ centered at $(-2, -2)$. This results in a steady periodic flow pattern.

Table 7: Numerical results for a circular container with $\Gamma = 8.38$ and a Gaussian deformation (a bump) at the bottom with $a = 0.05$ and $\sigma = 0.02$ and centered at $(-2, -2)$. The non-dimensional numbers were kept at $Ma = 105$, $Ra = 48$, and $Pr = 890$. In each of the 100 independent simulations a different random initial condition is imposed on the temperature.

Pattern	No. of cases
7 cell, stable	23
oscillatory	77

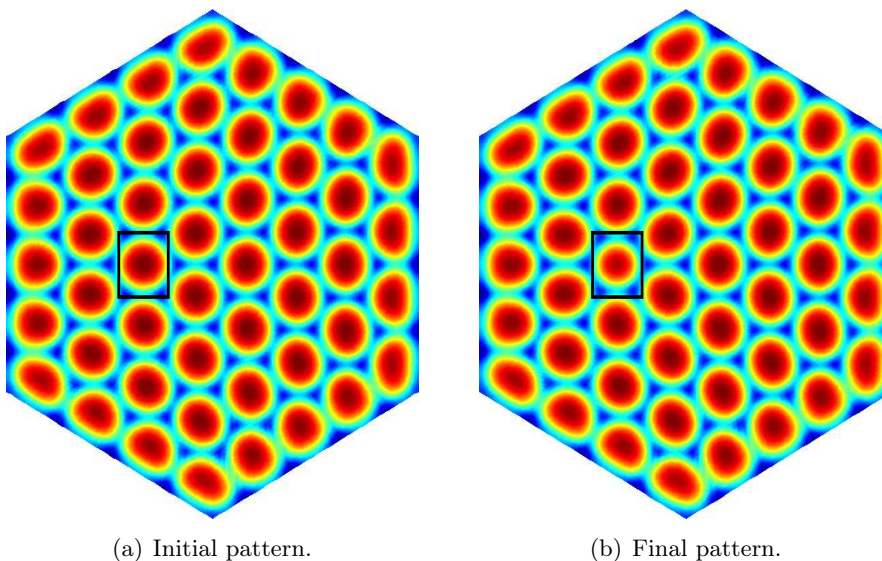


Figure 18: The resulting pattern from a simulation in a hexagonal container with $Ma = 105$, $Ra = 48$, $Pr = 890$, and $\Gamma = 22.0$. We have placed a small bump with $a = 0.05$ and $\sigma = 2.0$ centered at $(-5, 0)$. The simulation is started from a steady state pattern in a container without the bump, shown in the left plot. The system quickly evolves into the pattern shown in the right plot. The bump has no apparent effect on the global pattern; we can only notice it on the convection cell straight above the bump, which is slightly smaller than the rest of the cells in the pattern.

Next, we performed the same test using a “bump” with negative amplitude, i.e., instead of having a bump at the bottom of the container, we now have a dip. The results when starting from the ideal 48-cell convection pattern can be seen in Figure 19. These results are in line with those obtained for the bump: the only noticeable effect on the flow pattern seems to be localized to the cell strictly above the dip, with no apparent influence on the global flow pattern. The results when starting from a random initial condition for the temperature can be found in Figure 20(b). As in the case of a “bump”, we observe a somewhat irregular flow pattern.

We have also performed a few additional simulations starting from different random initial conditions for the temperature. All the patterns found after long time integration seem to deviate from the very regular hexagonal patterns observed in containers with

no deformations. The pattern may also include oscillatory cell(s), thus indicating that a geometry deformation can also have a destabilizing effect.

We have not been able to trigger defects in the regular convection patterns through the selected geometry deformations, in the sense of arriving at diamond shape cells/stars. This was not expected either since our deformations are non-trivial. What we have been able to demonstrate is that the system is more likely to be unstable, in the sense of settling into a steady periodic (oscillatory) state, in particular for smaller containers. If the amplitude of the deformations becomes sufficiently large, we have even been able to destabilize larger containers when starting from a regular hexagonal pattern associated with an undeformed container.

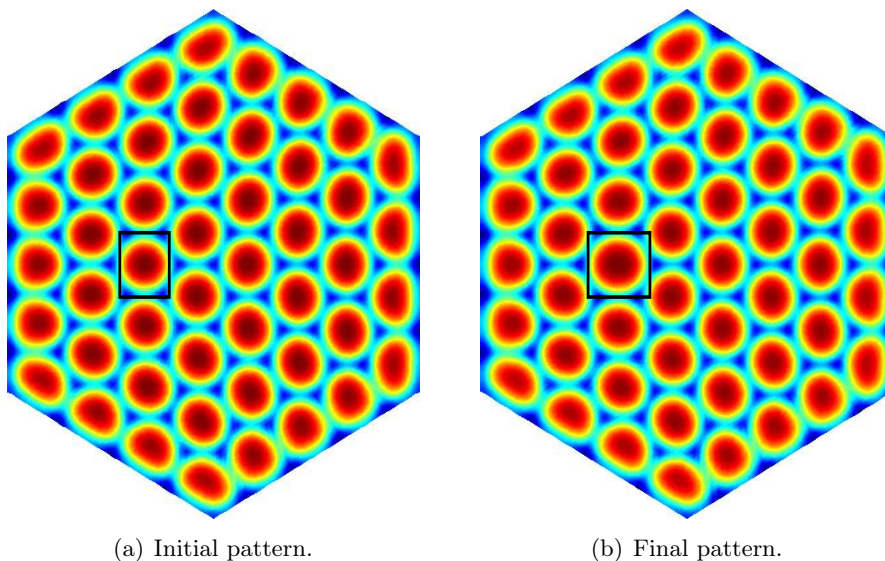


Figure 19: The resulting pattern from a calculation in a hexagonal container with $Ma = 105$, $Ra = 48$, $Pr = 890$, and $\Gamma = 22.0$. We have placed a small dip with $a = -0.05$ and $\sigma = 2.0$ centered at $(-5, 0)$. The calculation is started from a developed pattern in a container without the dip, shown in the left figure. The system quickly evolves into the pattern shown in the right plot. The dip has no apparent effect on the global pattern, we can only notice it on the convection cell straight above the dip, which is slightly larger than the rest of the cells in the pattern.

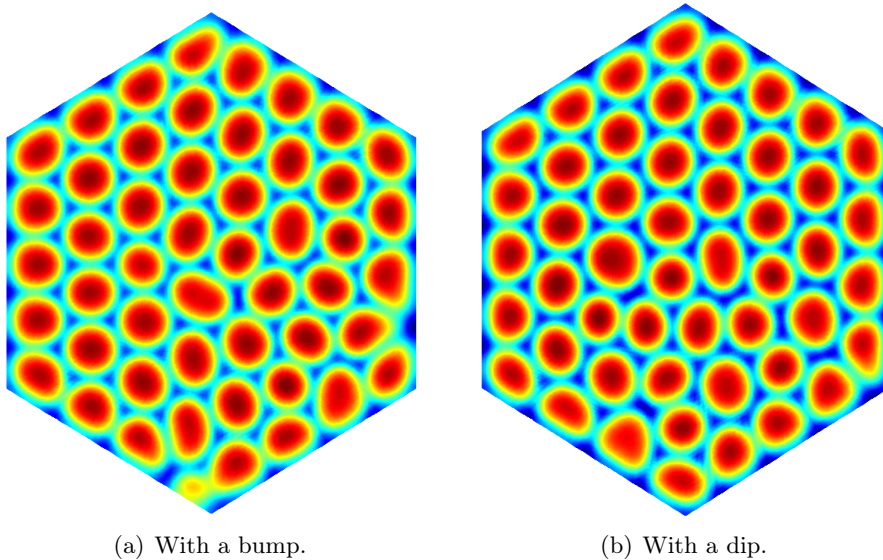


Figure 20: The resulting pattern from a simulation in a hexagonal container with $Ma = 105$, $Ra = 48$, $Pr = 890$, and $\Gamma = 22.0$. In the left picture we have placed a small bump with $a = 0.05$ and $\sigma = 2.0$ centered at $(-5, 0)$. In the right picture we have placed a small dip with $a = 0.05$ and $\sigma = 2.0$ centered at $(-5, 0)$. The simulations were started from random initial conditions. The systems evolved into the patterns shown, and remained in this state for about 800 units of dimensionless time.

8 Summary and conclusions

We have investigated the pattern formation in Bénard-Marangoni flows by numerically solving the incompressible Navier-Stokes equations coupled with a convection-diffusion equation for the temperature. The key parameters governing this problem are the Marangoni number, the Rayleigh number, the Prandtl number, and the global aspect ratio, Γ , of the three-dimensional container. We have considered Marangoni numbers higher than the critical number for the onset of convection rolls, but still in the vicinity of the critical number. Containers with circular, square and hexagonal cross-sections have been investigated. The main parameter we have varied has been the global aspect ratio. In addition, we have explored the effect of using different initial conditions.

Our main finding is related to the importance of the initial conditions for the system. Most of our simulations have been started with a zero initial velocity field and a random initial temperature field. For a given set of non-dimensional numbers, and for a given container, the system may evolve into more than one final state. For different random initial temperature fields, the final pattern may have a preferred state which is also consistent with experimental observations. However, the computational results indicate that there may exist several other final states for the system.

For example, the system may reach a steady state pattern which include different number of convection cells (and where one state is a preferred state). The system may also end up in a steady-periodic state in which one or more of the convection cells appear and disappear in an oscillatory fashion. We have also observed that the system may end up in a steady state where the pattern is quite regular over much of the domain, but with local

dislocations or irregularities, e.g., the formation of a star-like pattern in the middle of an otherwise hexagonal pattern. Such dislocations have also been observed experimentally, although they appear to be somewhat rare. It has been speculated in the literature that the reason for such irregularities in the pattern is imperfections in the geometry or the experimental setup. However, our simulations have shown that such dislocations may appear under otherwise ideal conditions. For a given set of non-dimensional numbers, and for a given container, we have shown that most of the simulations end up in a preferred state with a regular (hexagonal) pattern. Only on rare occasions will the system end up in a state with such dislocations. Again, the only difference between these simulations have been the use of different random initial conditions for the temperature field.

We have also investigated the case of symmetrizing the initial conditions for the temperature, e.g., imposing a square or octant symmetry, while otherwise using a random field within each quadrant or octant. Our results indicate that the initial symmetry will be broken as the system evolves to a final state. Still, this final state may be different compared to the state reached when starting with a completely random temperature field. In rare cases (for a container with a particular global aspect ratio), we have observed that the initial symmetry imposed at the start of the simulation is maintained until a final state has been reached.

Our final investigation relates to imposing a local Gaussian deformation at the bottom of the container. For a small circular container, we have observed that this causes the convection pattern to become more unstable, i.e., fewer cases end up in a steady state, and more cases end up in a steady-periodic (oscillatory) state. For a larger hexagonal container, we have performed tests indicating the sensitivity of the initial condition. If we use the steady state solution without a deformation as a (mapped) initial condition for a case with a deformation, the steady state pattern is only slightly changed (the cell above the deformation changes size). However, if we start from a completely random initial condition for the temperature, the system seems to evolve into a state without the very regular hexagonal pattern, but instead exhibit a much more irregular pattern, possibly including oscillatory cells.

9 Acknowledgment

The work has been supported by the Norwegian University of Science and Technology and the Research Council of Norway under contract 159553/I30 and contract 10323100. The support is gratefully acknowledged.

References

- [1] K. Arrow, L. Hurwicz, and H. Uzawa. *Studies in Nonlinear programming*. Stanford University Press, 1958.
- [2] H. Bénard. Les tourbillons cellulaires dans une nappe liquide transportant de la chaleur par convection en régime permanent. *Annales de Chimie et de Physique*, 23:62–144, 1901.
- [3] M. Bestehorn. Square patterns in Bénard-Marangoni convection. *Physical Review Letters*, 76:46–49, 1996.
- [4] T. Bjøntegaard, Y. Maday, and E. M. Rønquist. Fast tensor-product solvers: Partially deformed three-dimensional domains. *J. Sci. Comput.*, 39:28–48, 2009.
- [5] T. Bjøntegaard and E. M. Rønquist. A high order splitting method for time-dependent domains. *Computer Methods in Applied Mechanics and Engineering*, 197:4763–4773, 2008.
- [6] T. Bjøntegaard and E.M. Rønquist. Simulation of three-dimensional Bénard-Marangoni flows including deformed surfaces. *Communications in Computational Physics*, 5(2–4):273–295, 2009.
- [7] M. J. Block. Surface tension as the cause of Bénard cells and surface deformation in a liquid film. *Nature*, 178:650–651, 1956.
- [8] J. Bragard and G. Lebon. Non-linear Marangoni convection in a layer of finite depth. *Europhys. Lett.*, pages 831–838, 1993.
- [9] P. Cerisier, S. Rahal, and B. Billia. Extrinsic effects on the disorder dynamics of Bénard-Marangoni patterns. *Physical Review E*, 54:3508–3517, 1996.
- [10] P. Cerisier, S. Rahal, and N. Rivier. Topological correlations in Bénard-Marangoni convective structures. *Physical Review E*, 54:5086–5094, 1996.
- [11] S. Chandrasekhar. *Hydrodynamic and Hydromagnetic Stability*. Dover Publications, Inc., 1961.
- [12] A. Cloot and G. Lebon. A nonlinear stability analysis of the Bénard-Marangoni problem. *J. Fluid Mech.*, 145:447–469, 1984.
- [13] P. C. Dauby and G. Lebon. Bénard-Marangoni instability in rigid rectangular containers. *J. Fluid Mech.*, 329:25–64, 1996.
- [14] P. C. Dauby, G. Lebon, and E. Bouhy. Linear Bénard-Marangoni instability in rigid circular containers. *Physical Review E*, 56(1), 1997.
- [15] S. H. Davis. On the principle of exchange of stabilities. *Proceedings of the Royal Society*, 310:341–358, 1969.
- [16] S.H. Davis and G. Homsy. Energy Stability for Free-Surface Problems: Buoyancy-Thermocapillary Layers. *J. Fluid Mech.*, 98:527, 1980.
- [17] M. Van Dyke. *An Album of Fluid Motion*. Parabolic Press, Stanford, Ca., 1982.

- [18] C. W. Gear. *Numerical Initial value problems in ordinary differential equations*. Prentice-Hall, 1971.
- [19] W. J. Gordon and C. A. Hall. Construction of curvilinear co-ordinate systems and applications to mesh generation. *Intl. J. Numer. Meth. Eng.*, 7:461–477, 1973.
- [20] J. L. Guermond and J. Shen. On the error estimates for the rotational pressure-correction projection methods. *Math. Comp.*, 73:1719–1737, 2003.
- [21] E. L. Koschmieder. Bénard convection. *Advances in Chemical Physics*, 26:177–212, 1974.
- [22] E. L. Koschmieder. *Bénard Cells and Taylor Vortices*. Cambridge University Press, 1993.
- [23] E. L. Koschmieder and D. W. Switzer. The wavenumbers of supercritical surface-tension-driven Bénard convection. *J. Fluid Mech.*, 240:533–548, 1992.
- [24] E.L. Koschmieder and S.A. Prahl. Surface–tension–driven Bénard convection in small containers. *J. Fluid Mech.*, 215:571–583, 1990.
- [25] J. Kraska and R. Sani. Finite amplitude Bénard-Rayleigh convection. *Intl. J. Heat Mass Transfer*, 22:535–546, 1979.
- [26] A. M. Kvarving. A fast tensor-product solver for incompressible fluid flow in partially deformed three-dimensional domains: Parallel implementation. *In preparation*, 2010.
- [27] A. M. Kvarving, T. Bjøntegaard, and E. M. Rønquist. A fast tensor-product solver for incompressible fluid flow in partially deformed three-dimensional domains. *In preparation*, 2010.
- [28] Y. Maday and A. T. Patera. Spectral element methods for the incompressible Navier-Stokes equations. In *State-of-the-art surveys on computational mechanics (A90-47176 21-64)*. New York, American Society of Mechanical Engineers, pages 71–143, 1989.
- [29] Y. Maday, A. T. Patera, and E. M. Rønquist. An Operator-Integration-Factor Splitting Method for Time-Dependent Problems: Application to Incompressible Fluid Flow. *J. Sci. Comput.*, 5(4), 1990.
- [30] M. Medale and P. Cerisier. Numerical simulation of Bénard-Marangoni convection in small aspect ratio containers. *Numerical Heat Transfer, Part A*, 42:55–72, 2002.
- [31] K. Nitschke and A. Thess. Secondary instability in surface-tension-driven Bénard convection. *Physical Review E*, 52:5772–5775, 1995.
- [32] J. R. A. Pearson. On convection cells induced by surface tension. *J. Fluid Mech.*, 4:489–500, 1958.
- [33] M. L. Ramón, D. Maza, and H. L. Mancini. Patterns in small aspect ratio Bénard-Marangoni convection. *Physical Review E*, 60, 1999.
- [34] Lord Rayleigh. On convection currents in a horizontal layer of fluid when the higher temperature is on the under side. *Phil. Mag.*, 32:529–546, 1916.
- [35] S. Rosenblat, S. H. Davis, and G. M. Homsy. Nonlinear Marangoni convection in bounded layers - 1. circular cylindrical containers. *J. Fluid Mech.*, 120, 1982.

- [36] J. W. Scanlon and L. A. Segel. Finite amplitude cellular convection induced by surface tension. *Journal of Fluid Mechanics*, 30:149–162, 1967.
- [37] L. Schriener and C. Sternling. On cellular convection driven by surface-tension gradients; effects of mean surface tension and surface viscosity. *J. Fluid Mech.*, 21:321–340, 1964.
- [38] K. A. Smith. On convective instability induced by surface-tension gradients. *J. Fluid Mech.*, 24:401–414, 1966.
- [39] A. Thess and S.A. Orszag. Surface-tension-driven Bénard convection at infinite Prandtl number. *J. Fluid Mech.*, 283:201–230, 1995.
- [40] L. J. P. Timmermans, P. D. Mineev, and F. N. Van De Vosse. An approximate projection scheme for incompressible flow using spectral elements. *Intl. J. Numer. Met. Fluids*, 22, 1996.
- [41] D. J. Tritton. *Physical Fluid Dynamics*. Oxford Science Publications, 1988.
- [42] J. van Kan. A second-order accurate pressure-correction scheme for viscous incompressible flow. *J. Sci. Stat. Comput.*, 3, 1986.
- [43] S. T. Yu, B. N. Jiang, J. Wu, and J.C. Duh. Three-dimensional simulations of Marangoni-Bénard convection in small containers by the least-squares finite element method. *Comput. Methods Appl. Mech. Engrg*, 160:71–88, 1998.